ADVANCED MATERIALS
www.advmat.de

Manganese-Dioxide-Coating-Instructed Plasmonic Modulation of Gold Nanorods for Activatable Duplex-Imaging-Guided NIR-II Photothermal-Chemodynamic Therapy

*Ting He, Chao Jiang, Jin He, Yifan Zhang, Gang He, Jiayingzi Wu, Jing Lin, Xin Zhou, and Peng Huang**

Nanotheranostic agents of gold nanomaterials in the second near-infrared (NIR-II) window have attracted significant attention in cancer management, owing to the reduced background signal and deeper penetration depth in tissues. However, it is still challenging to modulate the localized surface plasmon resonance (LSPR) of gold nanomaterials from the first near-infrared (NIR-I) to NIR-II region. Herein, a plasmonic modulation strategy of gold nanorods (GNRs) through manganese dioxide coating is developed for NIR-II photoacoustic/magnetic resonance (MR) duplex-imaging-guided NIR-II photothermal chemodynamic therapy. GNRs are coated with silica dioxide (SiO_2) and then covered with magnesium dioxide (MnO_2) to obtain the final product of GNR@SiO_2@MnO_2 (denoted as GSM). The LSPR peak of GNRs could be tuned by adjusting the thickness of the MnO_2 layer. Theoretical simulations reveal that this plasmonic modulation is mainly due to the change of refraction index around the GNRs after coating with the MnO_2 layer. Additionally, the MnO_2 layer is demonstrated to degrade into Mn^{2+} ions in response to peroxide and acidic protons in the tumor microenvironment, which allows for MR imaging and chemodynamic therapy. This plasmonic modulation strategy can be adapted to other metal nanomaterials and the construction of a new class of NIR-II nanotheranostics.

1. Introduction

Optical imaging in the second near-infrared (NIR-II, 1000–1700 nm) window can achieve deeper tissue penetration and higher imaging contrast due to the lower photon scattering and background absorption than that done in the first near-infrared window (NIR-I, 650–950 nm).[1] Therefore, the development of theranostic agents in NIR-II region has become something of a research hotspot.[1a,2] Recently, there is an ever-increasing number of papers describing the modification of gold nanomaterials for NIR-II photoacoustic imaging (PAI) and photothermal therapy (PTT) owing to its unique plasmonic, acoustic, and electric properties, as well as multifunctionality endowed by its various dimensions and morphologies.[1c,e,3] Furthermore, its excellent biosafety surpasses the limits of most inorganic nanomaterials.[4] Currently, there are few methods that shift the localized surface plasmon resonance (LSPR) peak of gold nanomaterials from NIR-I to NIR-II region.[2a,5] For instance, some gold nanorods (GNRs) with superhigh aspect ratios or GNRs with extremely thin shells have been reported.[6] However, most of them still bear poor photostability. In fact, tailoring the morphology is not the only method to obtain a redshift in the absorbance of gold nanomaterials. Substances coated to the surface of GNRs can also cause absorbance red or blueshifts. For example, Wu et al. found that a layer of Cu_2O could cause absorbance redshift of GNRs from 600 to 800 nm.[7] Yeh et al. developed a rattle-like structure with a GNR encapsulated in a cavity of AuAg nanoshell to achieve a broad absorbance band span 300–1350 nm.[2a] However, most metal oxides suffer from biotoxicity and not responsive to tumor microenvironment. Therefore, the development of biocompatible and stimuli-responsive coatings for plasmonic modulation of GNRs remains a big challenge.

Manganese is one of the most commonly used metal element in cancer theranostics on account of its good biosafety and rich quantity of valence states, which allows for the design and synthesis of intelligent theranostic agents.[8] For example, manganese dioxide (MnO_2) is widely used as a catalase to decompose hydrogen peroxide (H_2O_2) in tumor microenvironment and produce oxygen and hence relieves the tumor hypoxia and reduces tumor resistance to radio- or chemotherapy.[9] Recently, it was reported that MnO_2 could decrease glutathione level in

Dr. T. He, C. Jiang, J. He, Dr. Y. Zhang, G. He, Dr. J. Wu, Prof. J. Lin, Prof. P. Huang
Marshall Laboratory of Biomedical Engineering
International Cancer Center
Laboratory of Evolutionary Theranostics
School of Biomedical Engineering
Shenzhen University Health Science Center
Shenzhen 518060, China
E-mail: peng.huang@szu.edu.cn
Prof. X. Zhou
Innovation Academy for Precision Measurement Science and Technology (APM)
Chinese Academy of Sciences (CAS)
Wuhan 430071, China
The ORCID identification number(s) for the author(s) of this article can be found under https://doi.org/10.1002/adma.202008540.

DOI: 10.1002/adma.202008540

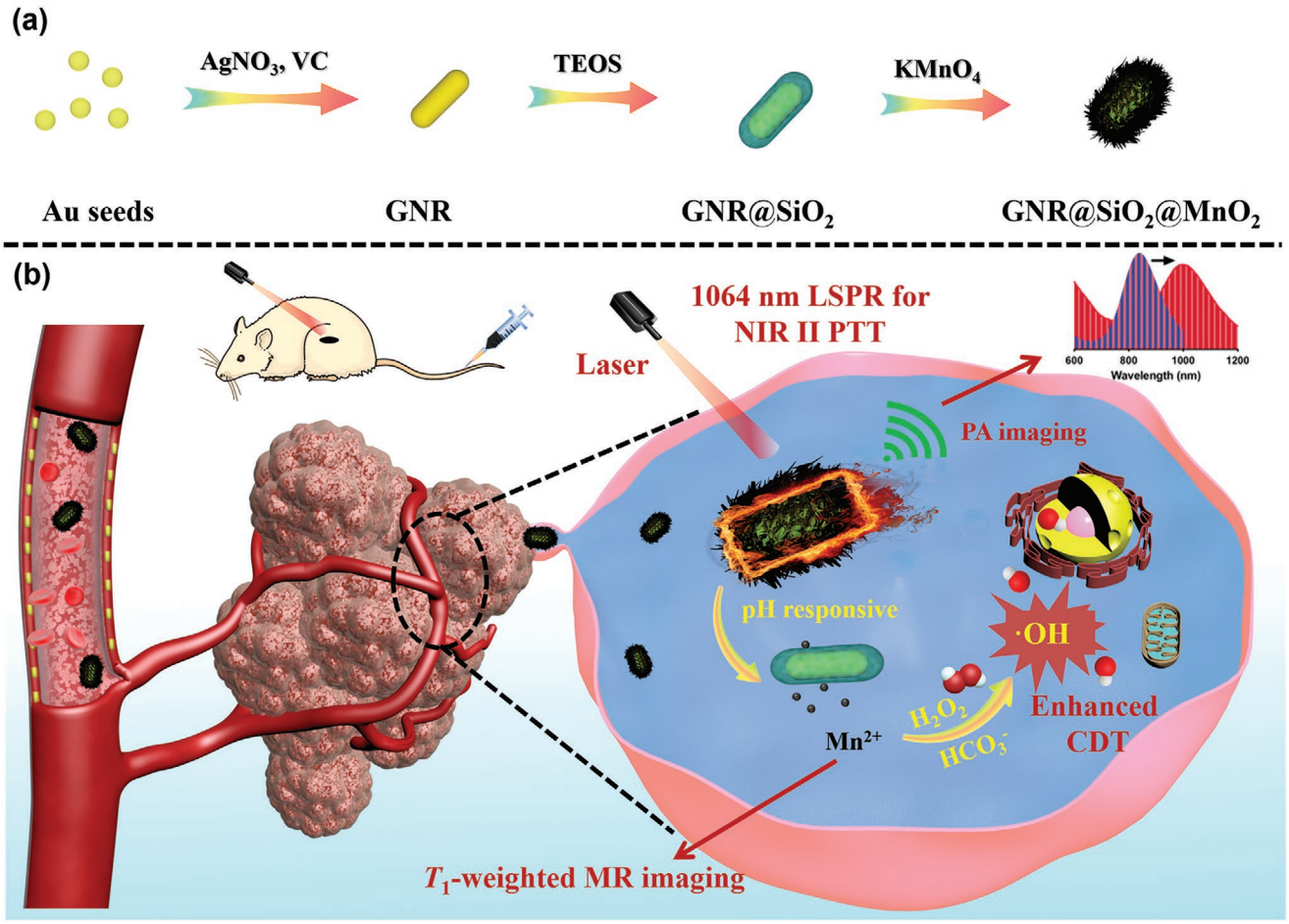

Scheme 1. a,b) Schematic illustrations of: a) preparation process of GSM nanotheranostic agent and b) tumor microenvironment-responsive PA/MR duplex imaging guided NIR-II photothermal-chemodynamic therapy.

the tumor microenvironment to enhance reactive oxygen species (ROS) level via the released manganese ions (Mn^{2+}), which mediated a Fenton-like reaction.[10] This Mn^{2+}-mediated chemodynamic therapy (CDT) further extends the potential of manganese as a nanotheranostic agent. In addition, Mn^{2+} is one of the best alternative contrast agents for T_1-weighted magnetic resonance imaging (MRI) besides gadolinium-based contrast agents. The high resolution and unlimited penetration depth of MRI could also make up for the limited imaging capability of PAI. Therefore, the integration of MnO_2 and GNRs is allows for the development of new multifunctional nanotheranostic agents.

Here, we developed a plasmonic modulation strategy of GNRs through MnO_2 coating for tumor microenvironment-responsive photoacoustic (PA)/magnetic resonance (MR) duplex imaging guided NIR-II photothermal-chemodynamic therapy (**Scheme 1**). The nanotheranostic agent, GNR@SiO_2@MnO_2 (denoted as GSM), was synthesized step-by-step (Scheme 1a). After coating with a MnO_2 layer, the LSPR peak of GNRs could be tuned from the NIR-I to NIR-II region. With the degradation of MnO_2 layer, GSM showed tumor microenvironment-responsive PAI and MRI. Moreover, Mn^{2+} released from GSM in the acidic tumor microenvironment catalyzed H_2O_2 into highly toxic hydroxyl radicals (•OH) for CDT (Scheme 1b).

2. Results and Discussion

The GNR seed was prepared by seed-growth approach and then the concentrations of vitamin C (VC) and $AgNO_3$ were adjusted to synthesize GNRs. Afterward, the prepared GNRs were cladded with a layer of silica oxide (SiO_2) on the surface by tetraethoxysilane (TEOS) hydrolysis reaction to obtain GNR@SiO_2 (GSs). Finally, a MnO_2 layer was grown on the outer layer through potassium permanganate ($KMnO_4$) decomposition method to obtain GNR@SiO_2@MnO_2 (GSMs) (**Figure 1**a). As shown in Figure 1b, a redshift in the UV–vis–NIR spectrum of GNRs from 670 to 850 nm was observed with the increase of aspect ratio. The transmission electron microscopy (TEM) images in Figure S1a in the Supporting Information showed that the average size of the GNRs was 60–75 nm (Figure 1c) and aspect ratio was arbitrarily adjusted to 2.46–4.05 by adjusting the amount of $AgNO_3$ from 90 to 110 µL and VC from 80 to 110 µL, respectively (Figure 1d). As shown in TEM images of GS, a uniform SO_2 layer was formed around the GNRs with a thickness of about 15 nm (Figure S1b, Supporting Information). No obvious absorbance change of GNRs was observed after SiO_2 coating (Figure 1e), which is probably because the silica layer causes a negligible change of refractive index around

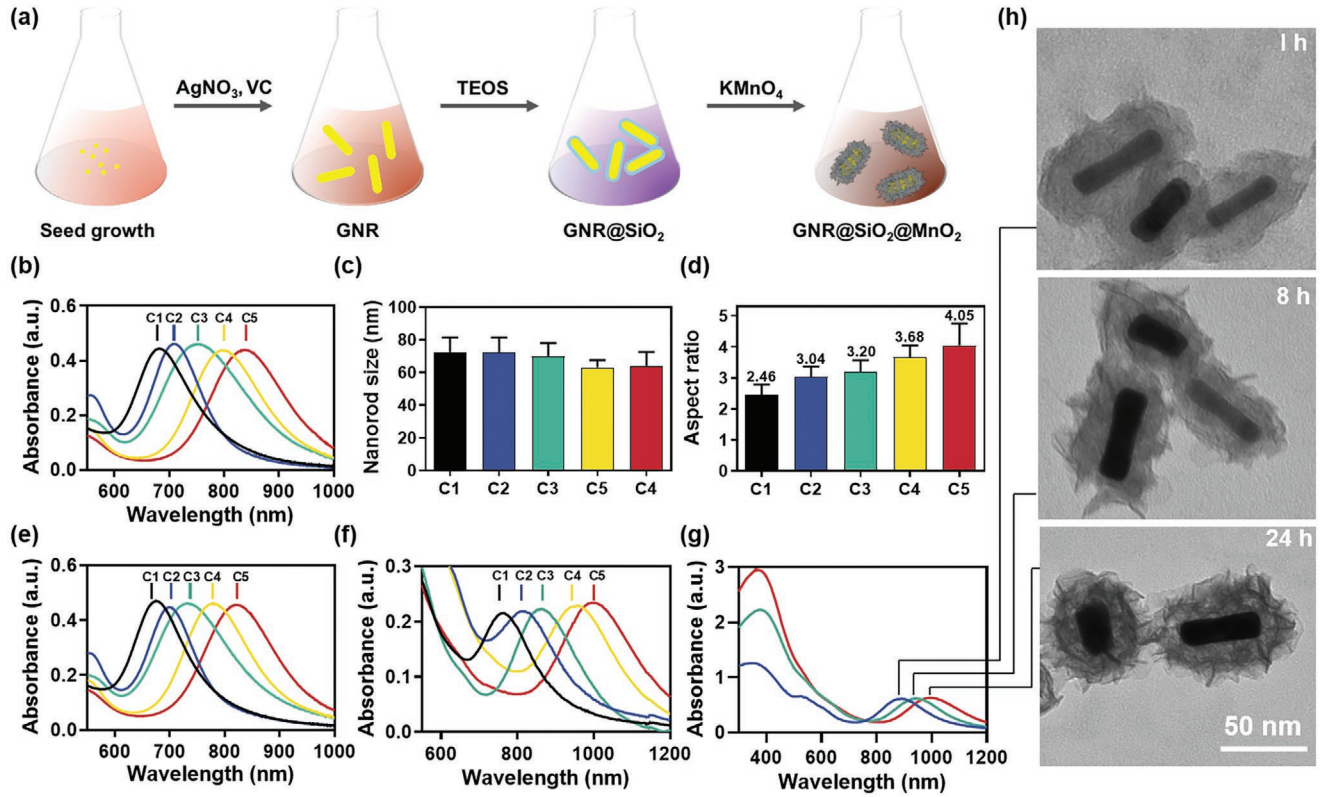

Figure 1. The preparation process of GSM and its absorbance in the NIR region tuned by MnO_2 layers. a) Scheme of the preparation process of GSMs by seed-mediated approach. b) UV–vis–NIR spectra of GNRs synthesized by different conditions (C1; C2; C3; C4; C5), c) their average length, and d) their aspect ratios measured by imageJ software. e) UV–vis–NIR spectra of GSs with different aspect ratios synthesized by TEOS hydrolysis reaction. f) UV–vis–NIR spectra of GSM with different aspect ratios synthesized after being clad with MnO_2 shells. g) The effect of MnO_2 layer thickness during the decomposition of $KMnO_4$ measured by UV–vis–NIR spectra and h) their TEM images at 1, 8, and 24 h.

GNRs. Figure S1c in the Supporting Information shows that an irregular MnO_2 layer is laminated on the surface of GSMs. Through this seed-mediated approach, the UV–vis–NIR absorption peak of GNR exhibited a redshift to 850 nm in the NIR-I region. Then, the GSMs were covered with a MnO_2 outer shell by ultrasonic thermal reduction of $KMnO_4$. Uniform GSMs were prepared when the ratio of GNR and $KMnO_4$ was adjusted to 1: 0.8 v/v, in which no extraneous MnO_2 sheets were formed according to the TEM images (Figure S2, Supporting Information). The as-prepared GSMs showed a redshift of ≈200 nm for all aspect ratios, resulting in an optimized absorbance peak at 1020 nm. An aspect ratio of 4.05 was chosen for the following experiments if not otherwise mentioned (Figure 1f) because it has the largest wavelength absorbance in the NIR II region. Furthermore, the thickness of MnO_2 layer also influenced the absorbance spectrum of GSM. As shown in Figure 1g,h, the thickness of MnO_2 flakes around GSMs increased over time from 1 to 24 h. The flaky morphology is the most common morphology obtained from the decomposition of $KMnO_4$. With the growth of MnO_2 layer, the characteristic absorbance of MnO_2 at 380 nm increased, and the absorption peak of GSMs also showed a redshift from 850 to 1020 nm, which indicated that the redshift of GSM is caused by the MnO_2 layer. These results showed that MnO_2 coating on the outer layer of GS can shift the absorption peak of GSMs to the NIR-II region.

To better understand the absorption redshift induced by MnO_2 coating, COMSOL simulation was conducted. The illustration of geometric parameters of GNR core and MnO_2 shells are listed in **Figure 2**a. Three core–shell structures were constructed by COMSOL software (Figure 2b). The refractive indexes of Au, MnO_2, and Ag were taken from Johnson and Christy.[11] The samples are dispersed in water and the surrounding refractive index of water is set to be 1.33. To simplify the model, the SiO_2 layer is omitted, which is based on the experimental observation that the absorbance of GS is not influenced by the SiO_2 layer. As shown in Figure 2c,d, the absorbance of GSM is redshifted to NIR-II region after MnO_2 coating, which is in parallel with those in Figure 1. With the thickness increase of MnO_2 layer on GNRs, a more redshifted LSPR was achieved. It shifted to 1050 nm when the thickness of MnO_2 layer reached 32 nm (Figure 2e). MnO_2 layers could significantly reduce the scattering intensity of GSM, which may be attributed to the electric shielding of MnO_2 shell. To compare, when the MnO_2 shell was replaced with Ag layer which has smaller refractive index than Au, the corresponding absorbance of GNR@SiO_2@Ag was blueshifted (Figure 2f). For example, the absorbance shifted from 850 to 720 nm, with a 2 nm of Ag layer. This is consistent with our previous observation that a dramatically blueshifted (≈120 nm) with silver deposition.[12] Collectively, these results suggested that it is the refractive

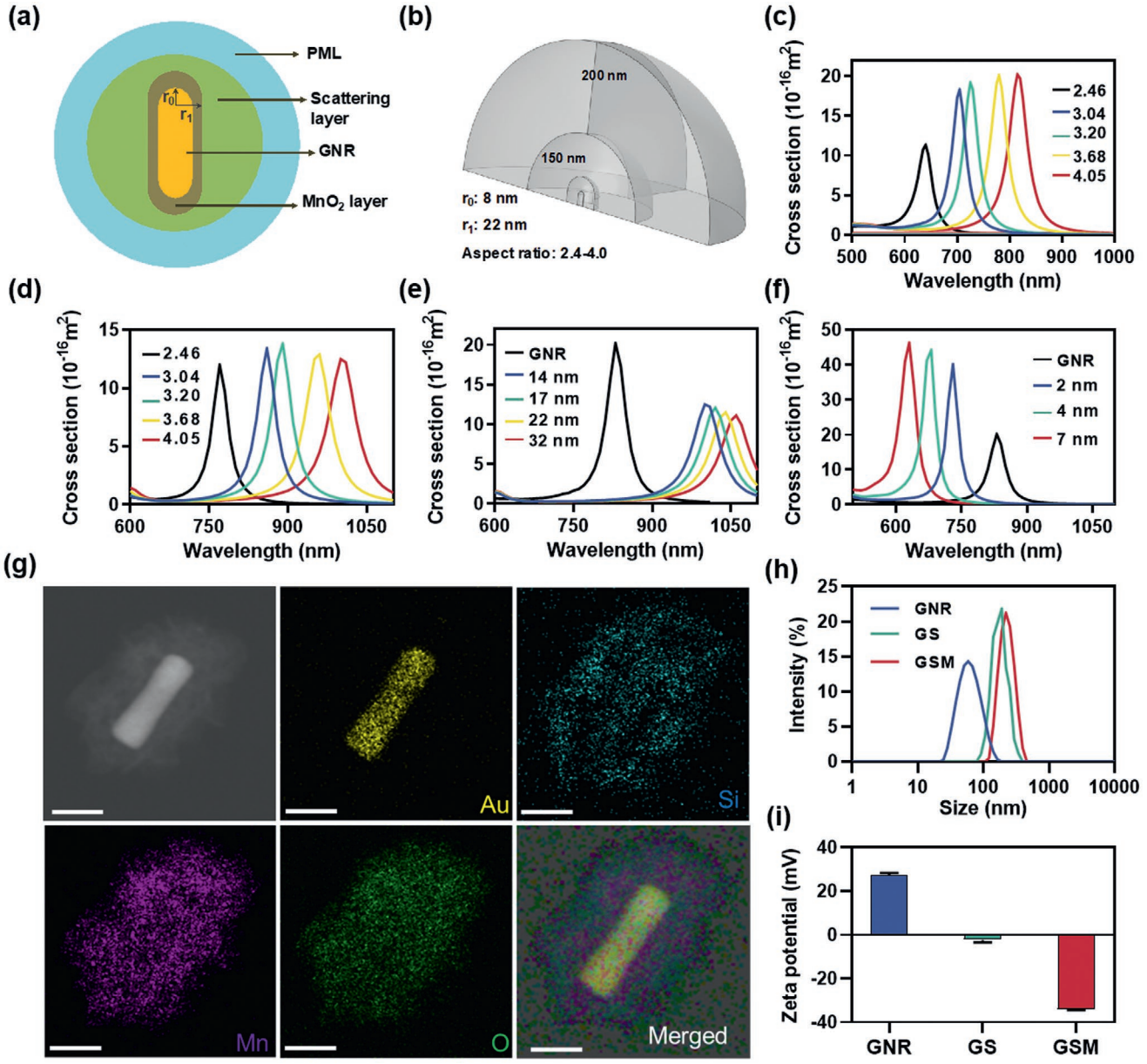

Figure 2. Simulations and associated calculations of modeled GSMs. a) Schematic illustrations of GSM for COMSOL simulation. b) Three core–shell structures of GSM constructed by COMSOL . r_1: 14, 17, 22, and 32 nm. c,d) Calculated SPR spectra of GNR (c) and GSM (d) at aspect ratios of 2.46, 3.04, 3.20, 3.68, and 4.05. e) Calculated SPR spectra of GSM with different shell thicknesses. f) Calculated surface plasmon resonance spectra of GNR@SiO_2@Ag with a Ag shell thickness of 2, 4, or 7 nm. g) Element mapping images of GSMs. Scale bar: 50 nm. h) Particle size determination by dynamic light scattering and i) zeta potential of GNR, GS, and GSM.

index of metal or metal oxide that determined the direction of absorbance shift of GNRs.

Next, the NIR II redshifted GSM was evaluated as a tumor microenvironment-responsive nanotheranostics. The dimension of GNR was about 15 nm × 65 nm, and the SiO_2/MnO_2 layer around GNR was nearly 30 nm. A core–shell like structure was showed in scanning transmission electron microscopy images of GSM (Figure S3, Supporting Information). Element mapping images showed that the Au core is surrounded with Si, Mn, and O elements (Figure 2g and Figure S4, Supporting Information). The hydrated diameters of GNR, GS, and GSM are 58, 190, and 220 nm, respectively (Figure 2h). Their zeta potentials are 27, −2, and −34 mV, respectively (Figure 2i). The particle size and negative potential of GSM are beneficial to subsequent in vivo experiments according to the nanoparticles size effect.

The photothermal capability of GSM in the NIR-II region was evaluated. As shown in **Figure 3**a GSM of 40 μg mL^{-1} still maintained nanorod structure after pulsed laser irradiation for 10 min. In contrast, the bare GNR become spherical particles due to melting and shape transition at high local temperature generated by pulsed laser irradiation.[13] The UV–vis–NIR spectrum

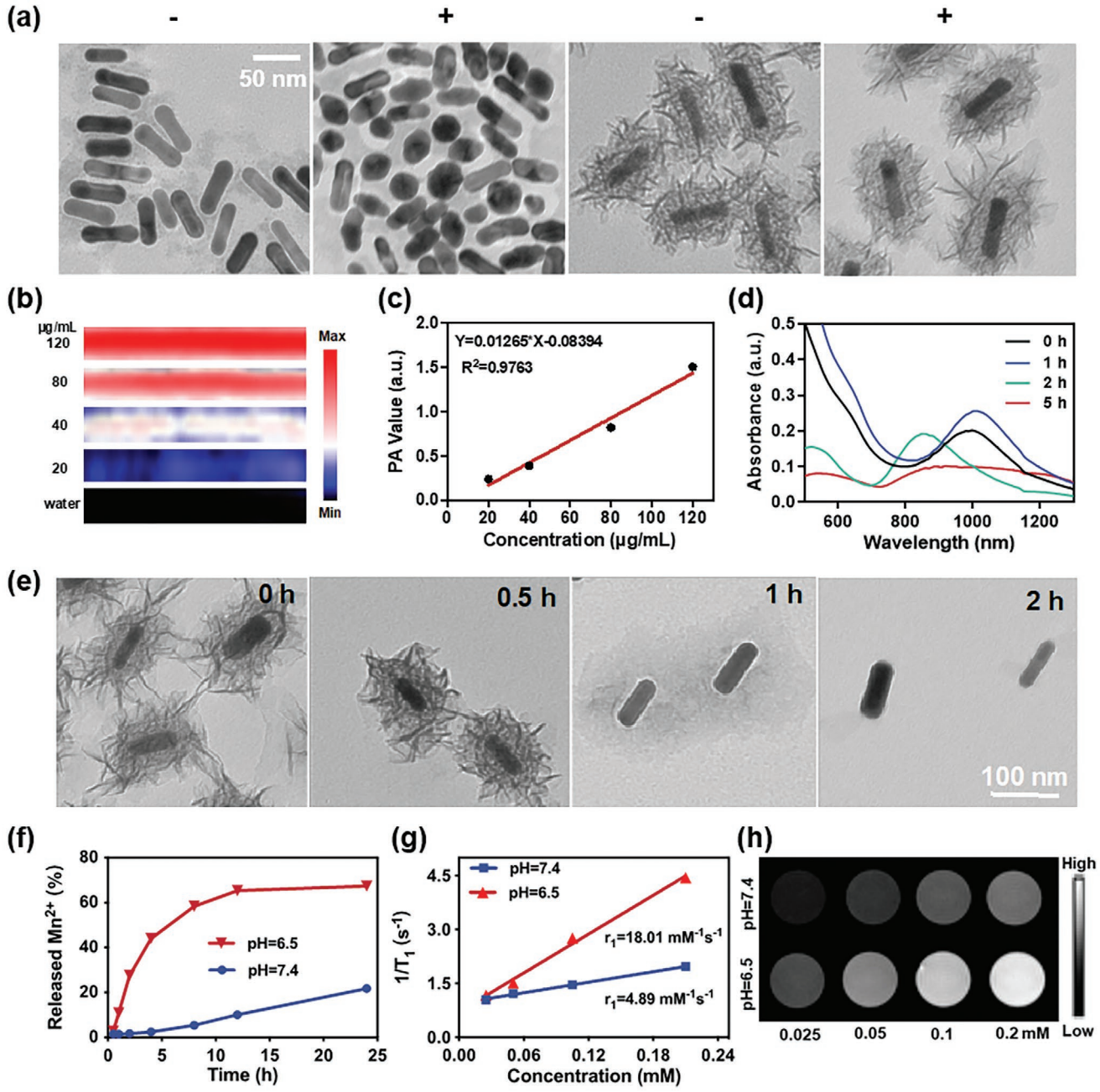

Figure 3. The stability and degradation properties of GSM. a) Morphologies of GSM and GNR before (–) and after (+) pulsed laser irradiation for 10 min. b) PAI images of GSM aqueous solutions in tubes in the concentration range of 0–120 μg mL^{-1}. c) The relationship between GSM concentration and PA value. d) UV–vis–NIR spectra of GSM in PBS (pH 6.5) at different time points, 0, 1, 2, and 5 h. e) TEM images of 40 μg mL^{-1} GSM after 0, 0.5, 1, and 2 h incubation in pH 6.5 PBS, respectively. f) Concentrations of the released Mn^{2+} from GSM over time at pH 6.5 and pH 7.4 buffer solution, respectively. g) The T_1 relaxivity and h) MRI images of GSM in the pH 6.5 and pH 7.4 buffer after 2 h incubation, respectively.

of bare GNR blueshifted from 800 to 700 nm after pulsed-laser irradiation, while that of GSM remain the same (Figure S5, Supporting Information). As shown in Figure S6a in the Supporting Information, the maximum temperature of GSM upon exposure to 1064 nm laser (0.4 W cm^{-2}, 5 min) is concentration dependent. As the concentration increased from 0 to 60 μg mL^{-1}, the peak temperature reached 52 °C, which is high enough to thermally ablate tumor cells. GSM of 40 μg mL^{-1} also exhibits similar power density dependence under different irradiation powers (Figure S6b, Supporting Information). A good photothermal stability of GSM is observed after six-cycle laser irradiation (Figure S6c, Supporting Information). The photothermal conversion efficiency of GSM is calculated to be 27.47% (Figure S6d, Supporting Information), which is slightly lower than that of reported bare GNR, but its photothermal stability is much better than that of GNR. Because of the excellent

photothermal stability, there is a good linear relationship between PA value and GSM concentration in the range of 20–120 μg mL^{-1}, which indicates a good PAI capability of GSM (Figure 3b,c).

The MnO_2 shell of GSM can be degraded in a low-pH environment. As shown in Figure 3d, UV–vis–NIR spectra of GSM exhibited a blueshift from 1020 to 850 nm in pH 6.5 buffer solution after 2 h incubation. Then a broad peak occurs after 5 h incubation, indicating that the degraded GSM aggregated. The color of GSM solutions gradually changed from brown-red to pink (Figure S7, Supporting Information). TEM images show that the MnO_2 shell becomes obscured and then disappears after 2 h incubation (Figure 3e). More than 68% of Mn^{2+} is released from GSM in buffer solution of pH 6.5 after 12 h incubation, but the proportion is only 15% in pH 7.4 solution (Figure 3f). Due to its acid sensitivity, GSM can perform MRI and CDT simultaneously. The longitudinal relaxation rate (r_1) of GSM is up to 18.01 mM^{-1} s^{-1} after 2 h incubation in pH 6.5 solution but only 4.89 mM^{-1} s^{-1} in pH 7.4 solution (Figure 3g,h). This significant difference indicates that GSM would be an excellent contrast agent for T_1-weighted MRI in acidic tumor microenvironment. All these results show the potential of GSM as a good tumor microenvironment-responsive NIR-II contrast agent for PAI/MRI.

As we know, Mn^{2+} can act as a Fenton-like agent to generate •OH with the assistance of HCO_3^- in tumor microenvironment. Methylene blue (MB), usually used as a dye that specifically degraded by •OH. As shown in **Figure 4**a the group of GSM + H_2O_2 + MB was completely degraded by •OH, but MB in other groups remained blue. The degradation of MB is concentration dependent (Figure 4b) and time dependent (Figure S8, Supporting Information). Encouraged by the above results, the therapeutic effect of GSM is evaluated on U87MG cell lines. In Figure 4c the cell viability slightly decreased when incubated with low concentration GSM (<20 μg mL^{-1}), but it dropped to 70% with 40 μg mL^{-1} GSM. It is supposed that the •OH catalyzed by Mn^{2+} mediated Fenton-like reaction increases the ROS level of U87MG cells. Thusly, we use an ROS probe 2′,7′-dichlorofluorescin diacetate (DCFH-DA) to detect the oxidative stress after being incubation with 0, 5, 10, and 20 μg mL^{-1} GSM. The nonfluorescent DCFH emits bright green fluorescent after being oxidized by intracellular ROS to 2′,7′-dichlorofluorescein. As the staining images showed, GSM at a concentration of 20 μg mL^{-1} significantly increases the oxidative stress in U87MG cells (Figure 4d), which is consistent with the cell viability results. To optimize the GSM incubation time, bio-TEM imaging for cell uptake and degradation of GSM (20 μg mL^{-1}) in U87MG cells are performed (Figure 4e). A large amount of GSM is observed in the endosomes after 4 h incubation, and the MnO_2 shells are degraded after 24 h incubation, indicating the successful cellular incorporation of GSM as well as the biodegradability of MnO_2 shells. Therefore, PTT in U87MG cells is conducted 4 h after incubation with GSM. The cell viability of GSM plus laser group decreases to 30% after laser irradiation (1064 nm, 0.4 W cm^{-2}) for 5 min (Figure 4a). After extending irradiation time to 10 min, the cell viability further decreases to less than 10%. Similar results are observed in cell live/death staining images (Figure 4f). Almost no living cells are observed after 10 min laser irradiation (1064 nm, 0.4 W cm^{-2}). All these in vitro results demonstrate the effective combination of PTT and CDT mediated by GSM on U87MG cells.

As shown above, GSM exhibits remarkable PTT/CDT combined therapeutic effects in vitro. Next, to maximize the in vivo therapeutic effect, we needed to confirm the tumor peak accumulation time of GSM in tumor tissues. Therefore, MRI and PAI are performed on the U87MG-tumor-bearing mice after intravenous (i.v.) injection with 5 mg kg^{-1} dose of GSM. The results shows that PA signal of tumor peaked at 4 h postinjection (p.i.), and the signal intensity is twofold stronger than that preinjection (**Figure 5**a,b). However, the strongest MRI signal is observed at 8 h p.i., which is 4 h later than that of PA signals (Figure 5c,d). It is supposed that GSM is gradually degraded in the acidic tumor microenvironment to release Mn^{2+}, which enhanced the MRI contrast of normal tissue and tumor, thus the MRI signals of GSM peaked at a later time than PA signals. The biodistribution of GSM in major organs and tumor tissues at 24 h p.i. was analyzed according to the content of Mn element by inductively coupled plasma atomic emission spectrometry (Figure S9, Supporting Information). Most of GSM were metabolized through the liver and spleen, and about 6.6% was accumulated in the tumor tissues.

Previous experiments show that the absorbance of GSM blueshifted after the MnO_2 layer of GSM degraded. To verify in vivo, GSM is intratumorally injected and the PA spectra of GSM in the tumor are recorded. A broad peak at 800–900 nm is observed after injection with GSM, which is divided into three peaks until 24 h p.i. (Figure S10, Supporting Information). This broad peak may be resulted from the incomplete degradation of GSMs. From the results of both PAI and MRI, the optimum time of PTT is set to be 4 h p.i. of GSM.

In vivo therapeutic effect of GSM was studied on U87MG-tumor-bearing mice. 20 mice are randomly divided into four groups: i) phosphate buffer solution (PBS), ii) GSM, iii) PBS + laser, and iv) GSM + laser. The injection dose was 5 mg kg^{-1}. At 4 h p.i., the tumors of laser groups were irradiated by a continuous-wave 1064 nm laser (0.8 W cm^{-2}) for 10 min. The tumor temperatures of GSM group and PBS group were recorded by a thermal imager. As shown in **Figure 6**a,b, the tumor temperature in GSM + laser group quickly reached above 50 °C under laser irradiation, while that of the control group showed no significant increase. This indicates that GSM could effectively accumulate in the tumor and generate hyperthermia upon exposure to laser irradiation. Then we monitored tumor growth of all four groups every 2 d during 12 d and normalized the tumor volumes in Figure 6c. While the control group shows a rapid tumor growth, a moderate suppression of tumor growth was observed in the GSM-treated group. Impressively, the tumors in GSM + laser group were completely eliminated without recurrence. The mice show a negligible weight change, indicating that GSM had negligible systemic toxicity (Figure 6d). Meanwhile, the survival spans of mice treated with GSM + laser were greatly prolonged (Figure 6e). After different treatments, tumor tissue in all treatment groups were separated for hematoxylin and eosin (H&E), Ki67, and terminal-deoxynucleotidyl transferase mediated nick end labeling (TUNEL) staining, respectively (Figure 6f). The tumors treated with NIR-II PTT/CDT show much more severe cell damages than other groups from the H&E staining images. Additionally, the expression of Ki67 is strongly associated with tumor cell proliferation and growth. From the Ki67 staining images, GSM

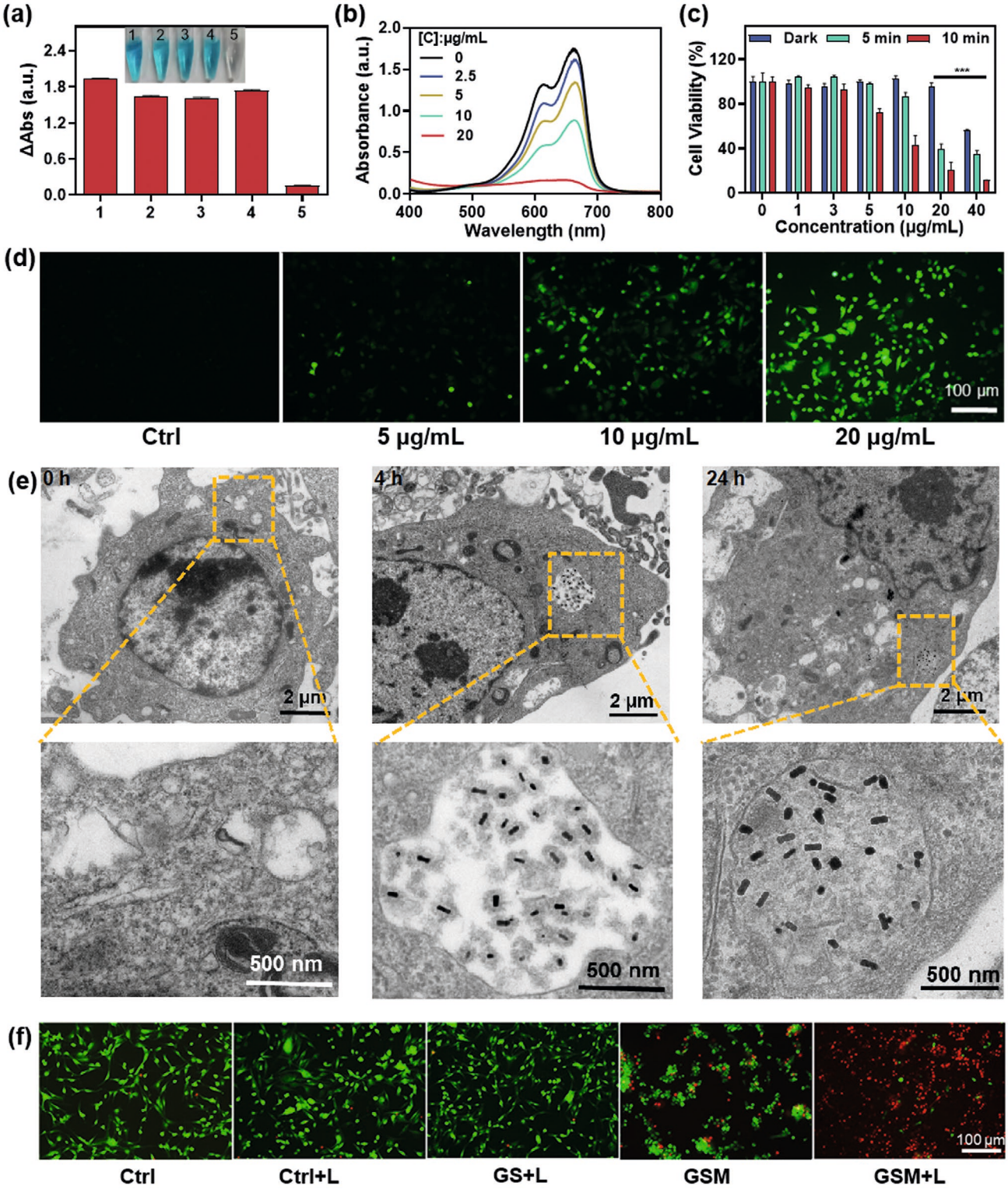

Figure 4. In vitro evaluation of CDT and PTT combined therapy. a) The absorbance of different solutions at 663 nm: 1) MB; 2) MB + H_2O_2; 3) MB + GSM (40 μg mL^{-1}); and 4) MB + H_2O_2 + GSM (40 μg mL^{-1}). b) The UV–vis–NIR absorption spectra of MB after adding different amounts of GSM to H_2O_2 (9×10^{-3} M)/$NaHCO_3$ (25×10^{-3} M)/MB mixed solutions. c) Viability of U87MG cells with different treatments: GSM + dark, GSM + 5 min laser, and GSM + 10 min laser. d) Fluorescence images of ROS staining of U87MG cells after being incubated with GSM. Scale bar: 100 μm. e) Bio-TEM images for cell uptake and degradation of GSM in U87MG cells 0, 4, and 24 h after being incubated with GSM (20 μg mL^{-1}). Scale bars: 2 μm (top) and 500 nm (bottom). f) Fluorescence images of calcein acetoxymethyl ester and propidium iodide staining on live/dead U87MG cells with or without laser treatment (1064 nm laser, 0.4 W cm^{-2}, 10 min) ([GS] = 20 μg mL^{-1}, [GSM] = 20 μg mL^{-1}). Scale bar: 100 μm.

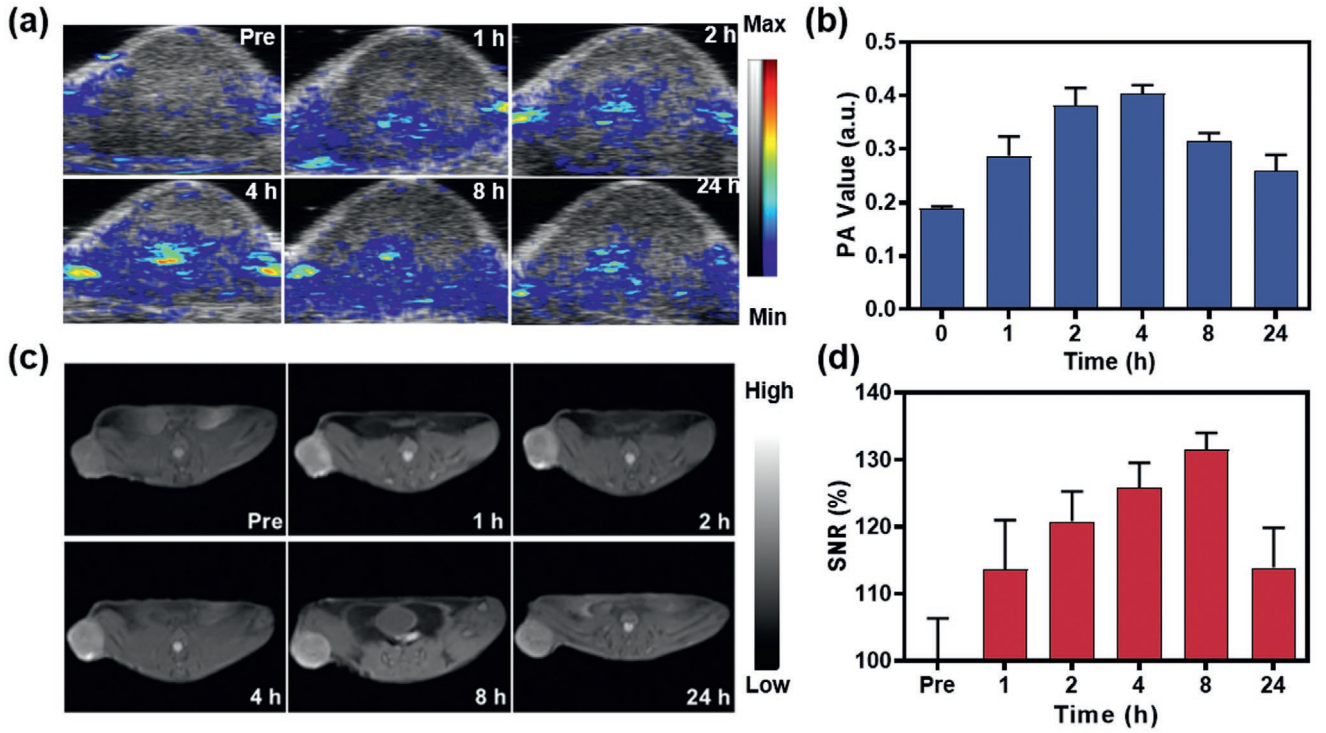

Figure 5. In vivo PAI and MRI evaluation of GSM. a) Representative PAI images of U87MG tumor 0, 1, 2, 4, 8, and 24 h postinjection with GSMs (5 mg kg^{-1}). b) The corresponding PA values of tumors in (c). Representative T_1-weighted MRI images of mice treated with GSMs 0, 1, 2, 4, 8, and 24 h postinjection with GSM. d) The corresponding signal to noise ratio analysis of MRI signals in tumors.

plus laser group shows very weak proliferation capacity. This result is consistent with the TUNEL staining images, which showed greater apoptotic signaling. According to the results of blood biochemistry, hematology analysis, and toxicity measurement of all major organs, GSM shows no obvious acute toxicity (Figures S11–S13, Supporting Information), indicating a good biocompatibility. Above results show a satisfying therapeutic outcome of GSM-mediated NIR-II PTT/CDT combination therapy, which has clinical application potentials.

3. Conclusion

A new plasmonic modulation strategy of gold nanomaterials through MnO_2 coating is explored. By adjusting the thickness of MnO_2 layer, the LSPR peak of GNRs can be tuned from the NIR-I to the NIR-II region. This plasmonic modulation is mainly due to the change in refraction index around GNRs according to the theoretical simulations. The as-prepared GSM with NIR-II plasmonic property can be used for NIR-II PAI and PTT. Furthermore, the MnO_2 layer can be degraded into Mn^{2+} ions in response to the elevated levels of H_2O_2 and H^+ in tumor microenvironment, which allow for MR imaging and CDT. This theranostic agent shows a significant increase of PAI signals after i.v. injected into U87MG-tumor-bearing mice and a slightly delayed increase in signal of T_1-weighted MR imaging. As an NIR-II theranostic agent, GSM exhibits excellent NIR-II PTT/CDT combination therapeutic effect after one-time treatment and good biological safety in both in vitro and in vivo experiments. This study provides a plasmonic modulation strategy of metal nanomaterials for biomedical applications, especially in the second near-infrared window.

Supporting Information

Supporting Information is available from the Wiley Online Library or from the author.

Acknowledgements

T.H. and C.J. contributed equally to this work. This work was financially supported by National Key R&D Program of China (2018YFA0704000), Guangdong Province Natural Science Foundation of Major Basic Research and Cultivation Project (2018B030308003), Basic Research Program of Shenzhen (JCYJ20180507182413022 and JCYJ20170412111100742), Shenzhen Science and Technology Program (KQTD20190929172538530), and Fok Ying-Tong Education Foundation for Young Teachers in the Higher Education Institutions of China (161032). The authors thank Instrumental Analysis Center of Shenzhen University (Lihu Campus). All animal experiments were performed under the regulations of the Animal Ethical and Welfare Committee of Shenzhen University (AEWC-SZU). U87MG cells were obtained from the Cell Bank of the Chinese Academy of Sciences (Shanghai, China).

Conflict of Interest

The authors declare no conflict of interest.

Data Availability Statement

Research data are not shared.

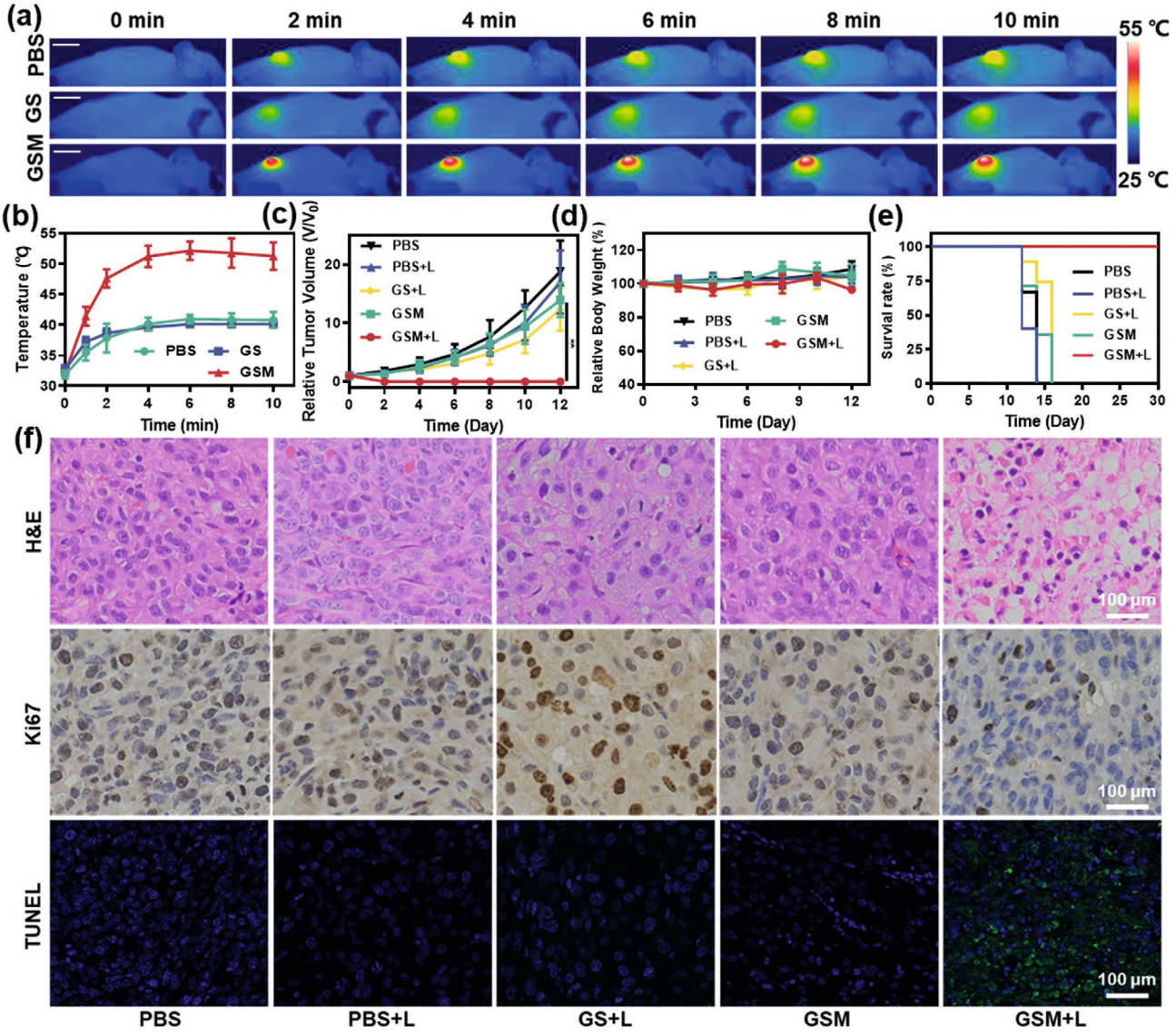

Figure 6. In vivo photothermal and therapeutic efficacies of GSM on U87MG-tumor-bearing mice. a) Representative thermographic images and b) average tumor temperatures of mice in different groups upon exposure to a 1064 nm laser 4 h postinjection with PBS, GS, and GSM. Scale bar: 1 cm. c) Normalized tumor growth curves of PBS, PBS + laser (PBS+L), GS+L, GSM, and GSM + laser (GSM + L) (mean and standard deviation, $n = 5$, $^{**}P < 0.01$). d) Body weights of groups during different treatments. e) The survival rate of mice after different treatments. f) H&E, Ki67, TUNEL staining images of tumor sections after different treatments. Scale bar: 100 μm.

Keywords

duplex imaging, gold nanorods, manganese dioxide, NIR-II, photothermal-chemodynamic therapy

Received: December 18, 2020
Published online: March 1, 2021

[1] a) Y. Cai, Z. Wei, C. Song, C. Tang, W. Han, X. Dong, *Chem. Soc. Rev.* **2019**, *48*, 22; b) A. L. Antaris, H. Chen, K. Cheng, Y. Sun, G. Hong, C. Qu, S. Diao, Z. Deng, X. Hu, B. Zhang, X. Zhang, O. K. Yaghi, Z. R. Alamparambil, X. Hong, Z. Cheng, H. Dai, *Nat. Mater.* **2016**, *15*, 235; c) W. Feng, X. Han, R. Wang, X. Gao, P. Hu, W. Yue, Y. Chen, J. Shi, *Adv. Mater.* **2019**, *31*, 1805919; d) Y. Zhang, S. Bo, T. Feng, X. Qin, Y. Wan, S. Jiang, C. Li, J. Lin, T. Wang, X. Zhou, Z. X. Jiang, P. Huang, *Adv. Mater.* **2019**, *31*, 1806444; e) C. Li, Y. Zhang, Z. Li, E. Mei, J. Lin, F. Li, C. Chen, X. Qing, L. Hou, L. Xiong, H. Hao, Y. Yang, P. Huang, *Adv. Mater.* **2018**, *30*, 1706150; f) Y. Jiang, X. Zhao, J. Huang, J. Li, P. K. Upputuri, H. Sun, X. Han, M. Pramanik, Y. Miao, H. Duan, K. Pu, R. Zhang, *Nat. Commun.* **2020**, *11*, 1857; g) X. Tang, L. Tan, K. Shi, J. Peng, Y. Xiao, W. Li, L. Chen, Q. Yang, Z. Qian, *Acta Pharm. Sin. B* **2018**, *8*, 587.

[2] a) M. F. Tsai, S. H. Chang, F. Y. Cheng, V. Shanmugam, Y. S. Cheng, C. H. Su, C. S. Yeh, *ACS Nano* **2013**, *7*, 5330; b) X. Yu, K. Yang, X. Chen, W. Li, *Biomaterials* **2017**, *143*, 120; c) Z. Cao, L. Feng, G. Zhang, J. Wang, S. Shen, D. Li, X. Yang, *Biomaterials* **2018**, *155*, 103; d) Q. Wang, Y. Dai, J. Xu, J. Cai, X. Niu, L. Zhang, R. Chen, Q. Shen, W. Huang, Q. Fan, *Adv. Funct. Mater.* **2019**, *29*, 1901480; e) C. Yang, M. R. Younis, J. Zhang, J. Qu, J. Lin, P. Huang, *Small*

2020, *16*, 2001518; f) J. Shao, J. Zhang, C. Jiang, J. Lin, P. Huang, *Chem. Eng. J.* **2020**, *400*, 126009; g) Z. Tang, P. Zhao, D. Ni, Y. Liu, M. Zhang, H. Wang, H. Zhang, H. Gao, Z. Yao, W. Bu, *Mater. Horiz.* **2018**, *5*, 946; h) K. Pu, J. Huang, *Angew. Chem., Int. Ed.* **2020**, *132*, 11813.

[3] a) J. Wang, J. Sun, Y. Wang, T. Chou, Q. Zhang, B. Zhang, L. Ren, H. Wang, *Adv. Funct. Mater.* **2020**, *30*, 1908825; b) H. Liu, G. Hong, Z. Luo, J. Chen, J. Chang, M. Gong, H. He, J. Yang, X. Yuan, L. Li, X. Mu, J. Wang, W. Mi, J. Luo, J. Xie, X. D. Zhang, *Adv. Mater.* **2019**, *31*, 1901015; c) W. Feng, X. Han, R. Wang, X. Gao, P. Hu, W. Yue, Y. Chen, J. Shi, *Adv. Mater.* **2019**, *31*, 1805919; d) Q. Q. Huang, Y. Zou, S. C. Zhong, X. Yang, J. Li, W. X. Huang, H. F. Zhu, C. Cheng, M. M. Ding, L. G. Zhu, Q. W. Shi, *J. Biomed. Nanotechnol.* **2019**, *15*, 910.

[4] a) T. S. Hauck, A. A. Ghazani, W. C. Chan, *Small* **2008**, *4*, 153; b) Q. Yang, J. Peng, K. Shi, Y. Xiao, Q. Liu, R. Han, X. Wei, Z. Qian, *J. Controlled Release* **2019**, *308*, 29.

[5] Y. S. Chen, Y. Zhao, S. J. Yoon, S. S. Gambhir, S. Emelianov, *Nat. Nanotechnol.* **2019**, *14*, 465.

[6] a) W. Zhang, K. Cai, X. Li, J. Zhang, Z. Ma, M. F. Foda, Y. Mu, X. Dai, H. Han, *Theranostics* **2019**, *9*, 4971; b) W. Li, X. Chen, *Nanomedicine* **2015**, *10*, 299.

[7] X. Shi, Y. Ji, S. Hou, W. Liu, H. Zhang, T. Wen, J. Yan, M. Song, Z. Hu, X. Wu, *Langmuir* **2015**, *31*, 1537.

[8] a) B. Ding, P. Zheng, P. Ma, J. Lin, *Adv. Mater.* **2020**, *32*, 1905823; b) Q. Chen, L. Feng, J. Liu, W. Zhu, Z. Dong, Y. Wu, Z. Liu, *Adv. Mater.* **2016**, *28*, 7129.

[9] a) W. Fan, W. Bu, B. Shen, Q. He, Z. Cui, Y. Liu, X. Zheng, K. Zhao, J. Shi, *Adv. Mater.* **2015**, *27*, 4155; b) C. R. Gordijo, A. Z. Abbasi, M. A. Amini, H. Y. Lip, A. Maeda, P. Cai, P. J. O'Brien, R. S. DaCosta, A. M. Rauth, X. Y. Wu, *Adv. Funct. Mater.* **2015**, *25*, 1858; c) Z. Wang, Y. Zhang, E. Ju, Z. Liu, F. Cao, Z. Chen, J. Ren, X. Qu, *Nat. Commun.* **2018**, *9*, 3334.

[10] a) L.-S. Lin, J. Song, L. Song, K. Ke, Y. Liu, Z. Zhou, Z. Shen, J. Li, Z. Yang, W. Tang, G. Niu, H.-H. Yang, X. Chen, *Angew. Chem., Int. Ed. Engl.* **2018**, *57*, 4902; b) T. He, X. Qin, C. Jiang, D. Jiang, S. Lei, J. Lin, W.-G. Zhu, J. Qu, P. Huang, *Theranostics* **2020**, *10*, 2453; c) L.-H. Fu, Y.-R. Hu, C. Qi, T. He, S. Jiang, C. Jiang, J. He, J. Qu, J. Lin, P. Huang, *ACS Nano* **2019**, *13*, 13985; d) Z. Tang, Y. Liu, M. He, W. Bu, *Angew. Chem., Int. Ed.* **2019**, *58*, 946.

[11] a) P. Johnson, R. Christy, *Phys. Rev. B* **1974**, *9*, 5056; b) P. B. Johnson, R. W. Christy, *Phys. Rev. B* **1972**, *6*, 4370.

[12] C. Jiang, Y. Huang, T. He, P. Huang, J. Lin, *Chem. Commun.* **2020**, *56*, 4942.

[13] G. Gonzalez-Rubio, A. Guerrero-Martinez, L. M. Liz-Marzan, *Acc. Chem. Res.* **2016**, *49*, 678.